Analysis of the Amplitude Response of a Two-Point and a Two-Line/Multi-Point Focused Laser Differential Interferometer

Brett F. Bathel*, Joshua M. Weisberger[†], Gregory C. Herring[‡] *NASA Langley Research Center, Hampton, VA, 23681*

Rangesh Jagannathan[§], Craig T. Johansen[¶] *University of Calgary, Calgary, Alberta, T2N 1N4, Canada*

Stephen B. Jones and Angelo A. Cavone**

Analytical Mechanics Associates, Inc., Hampton, VA, 23681

Experiments were performed with two different focused laser differential interferometer (FLDI) instruments to assess the amplitude response of each instrument to a traveling shockwave generated by a laser spark. The first FLDI instrument generated two measurement points, with each measurement point providing sensitivity to density fluctuations induced by the shockwave. By performing a cross-correlation between the signals obtained from each measurement point, the phase velocity of density fluctuations can be obtained. The second FLDI instrument generated two measurement lines that are oriented either parallel or orthogonal to the shockwave direction of travel with the resulting interference pattern sampled at multiple equally-spaced points along each line. As a result, this instrument provides density fluctuation measurement capability at multiple points simultaneously. When the measurement lines are oriented parallel to the shockwave direction of travel, the phase velocity, rate of change of the phase velocity, and acceleration of density fluctuations traveling along each line can be obtained by performing a cross-correlation between points along a single line. When the measurement lines are oriented orthogonal to the shockwave direction of travel, the spatially-varying phase velocity can be obtained by performing a cross-correlation between points at the same relative location on each measurement line. Computations of the shockwave generated by the laser spark are used to simulate the response of each instrument and are compared to the experimental results. High-speed schlieren imaging has also been performed and is compared with the FLDI measurements and computational results.

I. Nomenclature

FLDI = focused laser differential interferometer

 λ_0 = laser wavelength [nm]

 λ_{ρ} = density disturbance wavelength [mm]

 ρ = density [kg/m³]

 w_0 = laser beam waist radius [μ m] Δx_{NP} = Nomarski pair separation [μ m] Δx_{WP} = Wollaston pair separation [μ m]

^{*}Aerospace Technologist, Advanced Measurements & Data Systems Branch, Mail Stop 493, Senior Member AIAA.

[†] Aerospace Technologist, Advanced Measurements & Data Systems Branch, Mail Stop 493, Member AIAA.

[‡]Aerospace Technologist, Advanced Measurements & Data Systems Branch, Mail Stop 493.

[§]Ph.D. Candidate, Department of Mechanical & Manufacturing Engineering, 2500 University Drive NW.

[¶]Associate Professor, Department of Mechanical & Manufacturing Engineering, 2500 University Drive NW, Senior Member AIAA.

Research Technician, Advanced Measurements & Data Systems Branch, Mail Stop 493.

^{**}Research Technician, Advanced Measurements & Data Systems Branch, Mail Stop 493.

II. Introduction

The focusing laser differential interferometer (FLDI) originally described by Smeets and George [1] is capable of providing time-resolved measurements of density fluctuations at a point. The development of high-speed data acquisition systems in recent decades has allowed for the application of this instrument to high-speed supersonic and hypersonic flows [2–16]. Schmidt and Shepherd [17] developed a method to simulate the response of the FLDI instrument. In this work, they showed that an idealized disturbance field (sine wave) or CFD simulation could be used as an input to the simulation.

The purpose of this paper will be to simulate the amplitude response of several FLDI instrument configurations using methods similar to those in Ref. [18]. In this work, a traveling shockwave generated by laser-induced breakdown (LIB) spark will be used as the density disturbance. Since this disturbance can be considered as spherically symmetric, a 1-dimensional numerical simulation will be used to simulate the resulting flowfield. After validating the results of the numerical simulation against previously reported work [19] and high-speed experimental schlieren images obtained in this work, they will be used as the input to the FLDI instrument simulation. The time-varying signal obtained from the simulated FLDI instruments will then be compared against the signals obtained from experiment. Particular focus will be given to better understanding of the path-integrated nature of the FLDI instruments as well as issues with spatial averaging resulting from the finite size of the laser beams at their focus. If time permits, an analysis of effects of beam steering resulting from strong refractive index gradients in the flow will also be performed.

III. Experimental Setup

A. Two-Point FLDI Instrument

Figure 1 shows a schematic of the two-point FLDI system. On the pitch-side, a single-mode, linearly polarized $\lambda_0 = 532$ nm laser beam with a maximum power of 300 mW was directed onto the instrument's optical axis with a two-mirror (M^{1P} and M^{2P}) periscope. After the periscope, a half-wave plate (HWP^{1P}) followed by a polarizing beam-splitter (PBS) was used to adjust the laser power, with excess power directed into a beam dump (BD). A second half-wave plate (HWP^{2P}) then rotated the polarization axis of the laser by 45° with respect to the Nomarski prism's fast axis, and a subsequent 20 mm focal-length lens (BE) was used to diverge the beam. The diverging beam then passed through the Nomarski prism (NP) followed by a third half-wave plate (HWP^{3P}) that rotated the polarization axis of each diverging beam from the Nomarski pair by $\pm 45^{\circ}$ relative to the fast axis of a 2 arc-minute Wollaston prism (W^P), which further split each diverging beam into a Wollaston pair. A field lens (FL^P) consisting of two back-to-back 750 mm achromat doublet lenses (FL^{1P} and FL^{2P}) with an effective f-number of 7.4 then focused the diverging beams to a point in the test section corresponding to the instrument's measurement plane (section A-A in Fig. 1). These beams, with relative polarization directions denoted by the vertical and horizontal white lines, were oriented vertically on this plane as shown in Fig. 2. The use of the Nomarski prism ensured that the axis of each beam within the test section ran parallel to one another. More details on the use of this prism for two-point FLDI measurements can be found in Refs. [15, 16]. The resulting Nomarski and Wollaston pair separation on the measurement plane was $\Delta x_{\rm NP} = 2431 \pm 7 \,\mu{\rm m}$ and $\Delta x_{WP} = 257 \pm 9 \,\mu \text{m}$, respectively, while the waist radius of each beam was $w_0 = 26 \pm 7 \,\mu \text{m}$ at their focus. These measurements were obtained by imaging the intensity distribution of the focused laser light on the measurement plane with a small CMOS camera. A Gaussian fit to each focused beam was used to estimate the waist radius and identify each beam's center location within this plane.

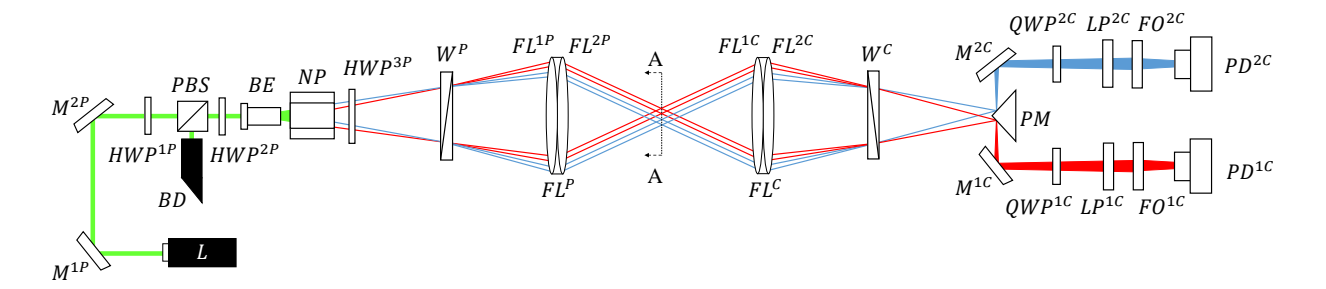


Fig. 1 Schematic of the optical setup for the two-point FLDI instrument.

On the catch-side, the field lens (FL^C) and Wollaston prism (W^C) arrangement mirrored that of the pitch-side about the measurement plane. After each Wollaston pair was made colinear by W^C, a knife-edge right-angle prism mirror (PM) was used to redirect each beam in the Nomarski pair in opposite directions. Each beam was then directed into separate quarter-wave plates (QWP^{1C} and QWP^{2C}) by a mirror (M^{1C} and M^{2C}, respectively), which were used to remove ellipticity in either beam's polarization state prior to an experiment. Separate linear polarizers (LP^{1C} and LP^{2C}) were subsequently used to pass the polarization angle corresponding to a phase offset of $\Delta\phi_{WP} = \pi/2$ between each Wollaston pair beam when no disturbances are present. Finally, a focusing optic (FO^{1C} and FO^{2C}) was used to loosely focus each beam onto a photodiode detector (PD^{1C} and PD^{2C}, respectively) with a rise time of 35 ns. The output voltages of each photodiode were recorded at 250 MHz during the experiment using a digital oscilloscope with 50 Ω termination.

As previously mentioned, the Nomarski and Wollaston pairs were oriented vertically on the measurement plane (section A-A in Fig. 1) as shown in Fig. 2. For the two-point FLDI measurements, a tightly-focused 532 nm pulsed laser beam was used to generate a laser-induced breakdown (LIB) spark at a point x = -66.7 mm above the two-point FLDI instrument's optical axis and aligned to both the Nomarski and Wollaston pair separation axes. The resulting shockwave from the LIB spark travelled parallel to the separation axes of the beam pairs as shown in Fig. 2.

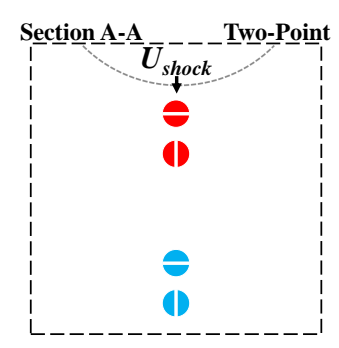


Fig. 2 Two-point FLDI laser light orientation on measurement plane.

B. Two-Line/Multi-Point FLDI Instrument

The two-line/multi-point FLDI instrument had an optical setup that was essentially identical to that of the two-point FLDI instrument with the exception of a few key optical component additions. In this instrument, a series of cylindrical lenses have been inserted at various positions along the instrument's optical axis so that lines of focused laser light are formed parallel to the vertical axis on the measurement plane. The first of these is a positive cylindrical lens, PCLP, that is placed so that it collimates the beams with respect to the vertical direction while allowing them to continue to expand in the horizontal direction. In Fig. 3, the magenta color is used hereafter to describe the propagation of the laser beams when viewed from the side. For reference, the coordinate system orientations for all colors used in the schematic are shown in the top left of Fig. 3. A Wollaston prism, WP, placed at the crossing point of the two beams formed by NP further splits each beam by 2 arc-minutes relative to the instrument's optical axis and parallel to the horizontal plane (top view). This creates two additional orthogonally-polarized beams. A negative cylindrical lens, NCL^P, is then placed one focal length from W^P to further expand the beam in the vertical direction. A field lens, FL^P, consisting of two back-to-back achromatic doublets, FL^{1P} and FL^{2P} , is used to focus the beams in the horizontal plane and collimate them in the vertical plane. This is placed at one effective focal length (EFL) from WP such that the central axis of each beam propagates parallel to one another and the instrument's optical axis after exiting FL^P. Using this configuration, two line pairs (each referred to as a Wollaston pair) are formed on the measurement plane (section A-A) as shown in Fig. 4a. Here, each line within each Wollaston pair is overlapped and aligned to the vertical axis, which is parallel to the direction of travel of the LIB shockwave (referred to hereafter as the parallel configuration. Here it is important to note that the length of the lines, ΔL , can be specified with careful selection of BE, PCL^P, and NCL^P focal lengths.

Beyond the measurement plane (section A-A) in Fig. 3, light from laser lines diverges in the horizontal direction and remains collimated in the vertical direction. A second field lens, FL^C , consisting of back-to-back achromatic doublets, FL^{1C} and FL^{2C} , is then placed at a distance from the measurement plane equal to that between FL^P and the measurement plane. For this work, both FL^P and FL^C are identical. After passing through FL^C , the beams are focused in both directions. Another 2 arc-minute Wollaston prism, W^C , is placed at the EFL of FL^C to combine the orthogonally-polarized beams from each Wollaston pair. The location of W^C also corresponds to the focus of the laser

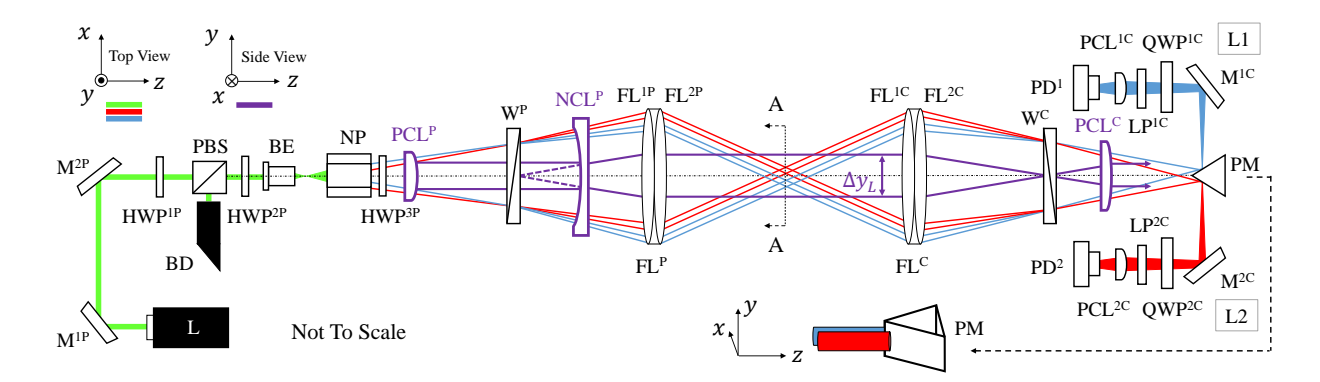


Fig. 3 Schematic of the optical setup for the two-line/multi-point FLDI instrument.

light in the vertical direction. After passing through W^C, the laser light begins to diverge in the vertical direction. This light is then collimated in the vertical direction by placing a positive cylindrical lens, PCL^C, one focal length from W^C. Beyond PCL^C the laser light from the Nomarski pair continues to converge in the horizontal direction until two focused laser lines are formed. The light from these lines, offset from one another by a small distance in the horizontal direction, are then split into two separate legs of the instrument, L1 and L2, with a right-angle prism mirror, PM. An isometric view of this splitting of the two laser lines with PM can be seen at the bottom right of the schematic. After PM, both legs L1 and L2 contained the same optical components. First a turning mirror, M^{#C}, redirects the beam by 90° and can be adjusted for alignment on to the detector. The beam then passes through a quarter-wave plate, QWP^{#C}, that is adjusted to remove any ellipticity in the polarization of the beam. Next a linear polarizer, LP^{#C}, makes the two overlapping orthogonally-polarized beams interfere with one another, and a short focal length positive cylindrical lens, PCL^{#C}, is used to adjust the thickness of the laser line incident on the linear silicon PIN photodiode array, PD[#]. Here it is important to note that careful selection of the focal length of PCL^C determines the length of the laser line incident on PD[#]. For the experiments described in this work a 16-element silicon PIN photodiode array was used, with each element measuring 0.8 mm high (active area 0.7 mm) for a total height of 12.8 mm and a total width of 2.0 mm. Therefore, the focal length of PCL^C was selected in order to slightly overfill PD[#] in the vertical direction.

The orientation of the laser lines can be changed to address the particular measurement needs for a flow. Figure 4b shows a second possible laser line orientation that can be achieved with this instrument. Here, NP is then rotated such that the each Wollaston pair is separated in the vertical rather than horizontal direction. All of the cylindrical lenses are then rotated by 90° such that the lines are parallel to the horizontal axis and orthoganl to the direction of travel of the LIB shockwave. Additionally, the PM and all subsequent optics in legs L1 and L2 were mounted together and connected with a rotation mount to the catch side of the instrument so that they could all be rotated by 90° about the instrument's optical axis to capture the light from the orientation shown in Fig. 4b. This alternative configuration is referred to hereafter as the *orthogonal configuration*.

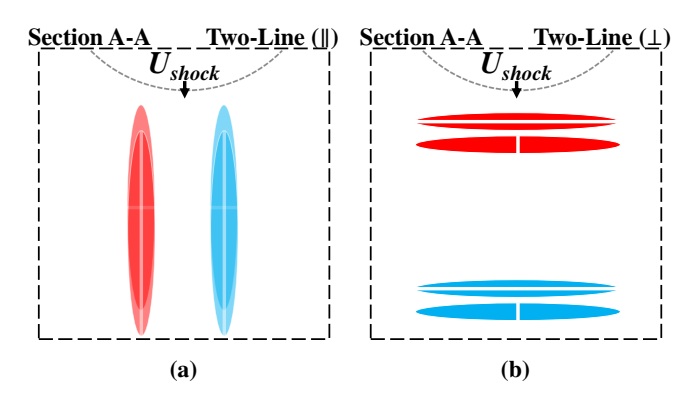


Fig. 4 Two-line/multi-point FLDI (a) parallel and (b) orthogonal configurations on measurement plane.

The time-varying current signals from the photodetector elements were terminated at 50 Ω and simultaneously

digitized at 14-bit resolution using two 8-channel high-speed oscilloscope modules with the receipt of an external trigger pulse. While each channel had a bandwidth of 250 MHz, data were acquired at 50 MHz on each channel.

C. High-Speed Schlieren Imaging

For all experiments, a high-speed schlieren imaging system was oriented orthogonal to the FLDI instrument's optical axis as shown in Fig. 5. A pulsed green LED was used as the schlieren light source. Figures 5a and 5b show a top and side view schematic of the schlieren imaging system setup, respectively. The left schematics in Fig. 5 show how the laser light is focused for the two-point FLDI instrument, represented by the red and blue lines, relative to the schlieren field-of-view (FOV). This is the configuration shown in Fig. 2. The middle and right schematics in Fig. 5 shows how the laser light is focused for the parallel and orthogonal two-line/multi-point FLDI configurations, respectively, relative to the schlieren FOVs. These correspond to the configurations shown in Figs. 4a and 4b, respectively. In this work, the schlieren images were used to visualize the shockwave and trailing expansion region resulting from the spark as they passed through the FLDI instrument's measurement plane. For the two-point FLDI measurements, a framing rate of 200 kHz was used. For the two-line/multi-point FLDI measurements, a framing rate of 400 kHz was used. For all experiments, the knife-edge of the schlieren system was placed parallel to the front surface of the shockwave. The FLDI data acquisition system also recorded a synchronization signal from the camera for comparison of the relative schlieren signal intensities to the relative FLDI signal intensities from each Wollaston pair.

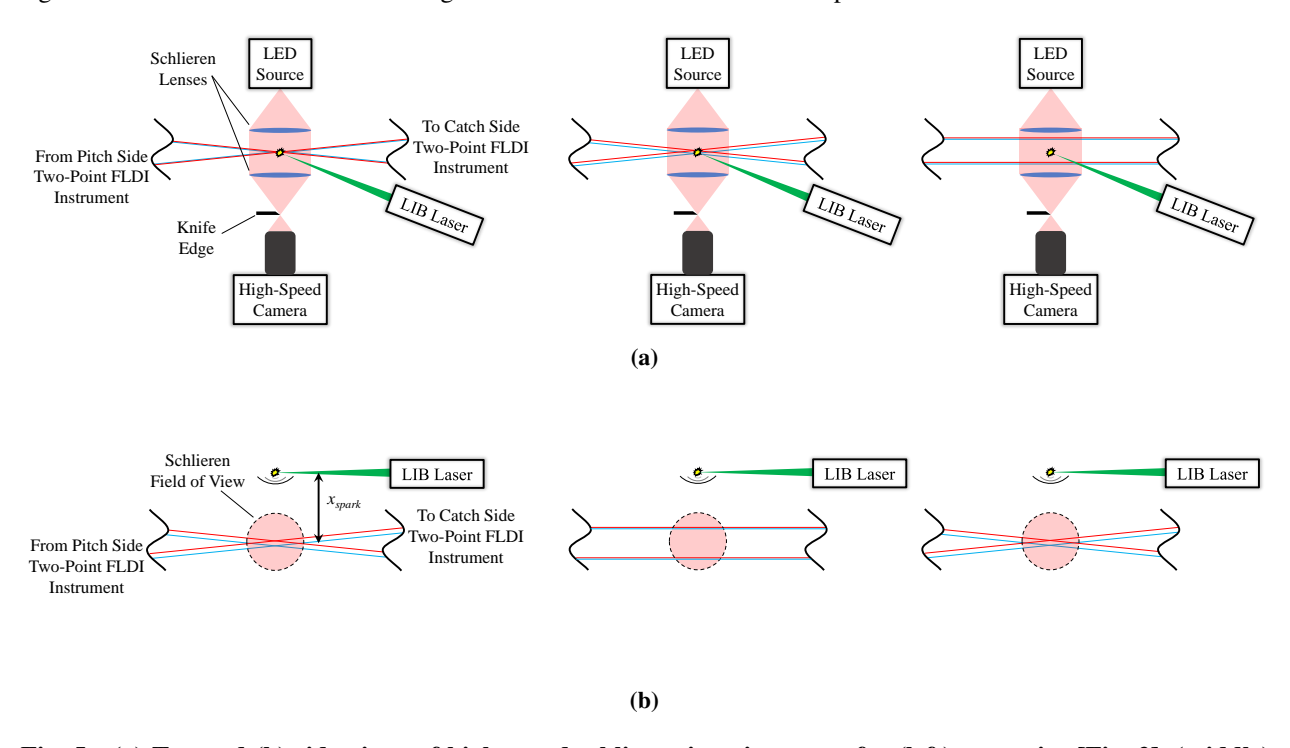


Fig. 5 (a) Top and (b) side views of high-speed schlieren imaging setup for (left) two-point [Fig. 2], (middle) two-line parallel [Fig. 4a], and (right) two-line orthogonal [Fig. 4b] FLDI instrument configurations.

IV. Numerical Simulation Details

A. Laser-Induced Breakdown Spark Shockwave Computations

Simulations of the shockwave resulting from a LIB spark were performed using the *rhoCentralFoam* solver in OpenFOAM [20]. For this work, the flowfield was assumed to be spherically symmetric and so only a 1-dimensional grid was used for the simulation. The grid consisted of 20,000 cells uniformly distributed in the radial direction with a cell spacing of 5 μ m. A grid convergence study was performed to ensure no dependence of the solution on the grid spacing. The pressure and temperature were initially set to 101,325 Pa and 293 K throughout the domain. A constant specific

heat of $C_p = 1005$ kJ/(kg·K) and constant viscosity of $\mu = 1.81 \times 10^{-5}$ Pa·s were assumed. A Kurganov-Tadmor scheme was used for flux terms and Crank-Nicolson method for time derivatives. Deposition of thermal energy from the laser spark was handled according to the methods outlined Yan *et al.* [19]. The final version of the paper will include a more detailed comparison to results in Ref. [19] to verify the accuracy of the simulation performed.

B. FLDI Instrument Simulation

To simulate the response of the two-point FLDI instrument, a polar grid similar to that specified by Schmidt and Shepherd [18] will be evenly spaced along the optical axis of each beam. A example of this grid is shown in Fig. 6a at the measurement plane. As in Ref. [18], the polar grid extends to twice the local Gaussian beam radius, with radial grid points spaced from the outermost radial point according to:

$$r_k = r_{k-1} \left(\frac{2 - \delta \theta}{2 + \delta \theta} \right) \tag{1}$$

where $r_1 = 2w$, $r_{N-1} \approx w/1000$ (with a total number of N radially-spaced grid points), and $\delta\theta = 2\pi/300$ is the spacing of the grid in the azimuthal direction in units of radians. An additional grid point is placed at $r_N = 0$.

For the two-line/multi-point FLDI simulation, a different gridding approach will be used to ensure that the signal terminating on each simulated photodiode element in the linear array will include an equal number of grid points. Figure 6b shows a portion of the grid used to simulate the FLDI line instrument. For this grid, both minor $(w_{minor} \approx 10 \ \mu \text{m})$ and major $(w_{major} \approx 4757 \ \mu \text{m})$ waist radii are specified as the actual focused lines are best represented by an ellipse. Here, the grid spacing along the major axis is kept constant according to:

$$\Delta \tilde{x} = \frac{V}{500} \tag{2}$$

where V is the vertical height of each photodiode element on the linear photodiode array. Using the equation for an ellipse, the outermost grid point at each \tilde{x} point along the major axis of the line is:

$$\pm \tilde{y}_1 = B_1 \sqrt{1 - \left(\frac{\tilde{x}}{2w_{major}}\right)^2} \tag{3}$$

where $B_1 = 2w_{minor}$ for the outermost grid points. Finally, the inner grid spacing at each \tilde{x} point along the major axis is defined as the intersection of successively smaller ellipses with minor axes specified as:

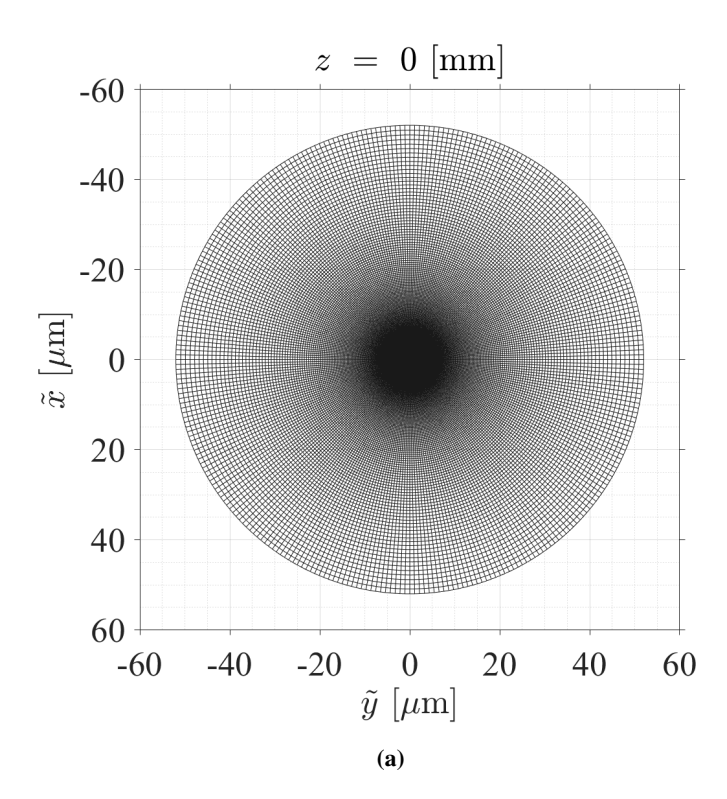
$$B_{k} = B_{k-1} \left(\frac{2V N_{e} \frac{w_{minor}}{w_{major}} - \Delta \tilde{x}}{2V N_{e} \frac{w_{minor}}{w_{major}} + \Delta \tilde{x}} \right)$$
(4)

The top-left image in Fig. 7 shows the placement of two-point FLDI simulation grids along the instrument's optical axis. Note that the spacing shown here is only notional and does not reflect the true grid spacing that will be used in the final analysis. The remaining images in Fig. 7 show results from the numerical simulation of the shockwave beginning at $t = 174 \,\mu \text{s}$ in 5 μs time steps (up to 214 μs) after the initial LIB spark. In these images, both the plane orthogonal to the schlieren FOV (xz plane at y = 0) and those co-planar to the FLDI simulation grids (xy planes) are shown. Here, the expansion of the shockwave can be observed.

V. Results

A. Comparison of Schlieren and Numerical Simulations

Figure 8 shows a comparison between the shockwave simulated in OpenFOAM and the high-speed schlieren images beginning at $t \approx 147~\mu s$ after the initial LIB spark in 5 μs time increments. Here, the results from the numerical simulation are shown on the left ($y \leq 0$) and the experimental schlieren images on the right (y > 0). Scattered light from each Wollaston pair of the two-point FLDI instrument is shown in green false-color in each image. This scattered light was generated by spraying canned air near the focus of the instrument, which was then imaged by the high-speed schlieren camera when no LIB shockwave present. It should be noted that the simulation results represent the density field while the schieren images are representative of the path-average vertical density gradient field. These images show



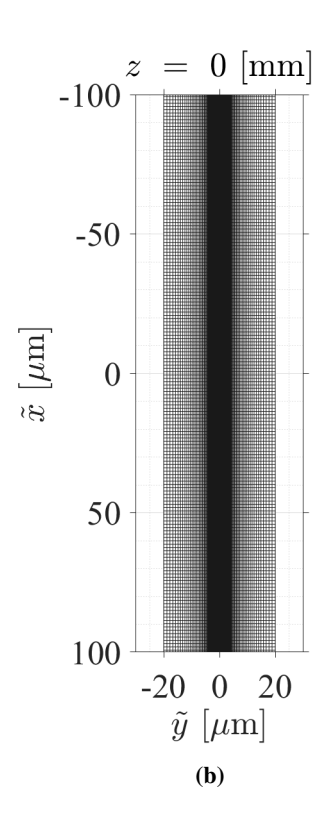


Fig. 6 Cross-sectional view of (a) two-point and (b) two-line/multi-point FLDI simulation grids at the z=0.

that the numerical simulations accurately capture the propagation speed and location of the initial shockwave generated by the LIB spark. In the final version of the paper, an effort will be made to compute numerical schlieren images from the simulations so that a more direct comparison with the experimental schlieren images can be made so that a more thorough validation of the numerical simulation can be made.

B. FLDI Measurements

Figure 9a shows the signals obtained from the two-point FLDI instrument. Here, the red and blue line colors correspond to the Wollaston pair locations shown in Fig. 2. In the final paper, results from the FLDI instrument simulation using the numerical simulation of the shockwave as an input will be compared against these experimental signals. An attempt will be made to understand the sensitivity of the instrument to disturbances away from the focus. Additionally, we will compare the results obtained with the two-point FLDI instrument to results obtained with high-speed schlieren imaging. A comparison of the velocities obtained with each method and from the numerical simulation will also be made.

Figure 9b shows the signals obtained from the 16-channel linear photodiode array for the two-line/multi-point FLDI instrument with the parallel configuration shown in Fig. 4a. Here, only a measurement from a single line in the parallel configuration is shown. The darker curves correspond to measurements made closer to the initial laser spark. As the shockwave continues to travel through the focused laser line, the downstream photodiode elements begin to register signal from the shockwave. The variation in peak amplitude registered on each element demonstrates the Gaussian intensity distribution of the light along the major axis of the focused laser line. In the final paper, results from the FLDI instrument simulation will be compared against these experimental signals to better understand the response of the two-line/multi-point FLDI instrument will using this configuration.

Figure 9c shows the signals obtained from two 16-channel linear photodiode arrays for the two-line/multi-point FLDI instrument with the orthogonal configuration shown in Fig. 4b. Here, only measurements from the even channels on each linear photodiode array were obtained. This allowed for shockwave velocities to be obtained at several points as well as the curvature of the shockwave to be determined by measuring the time of arrival of the shockwave at each element. Figure 9d shows a zoomed-in view of the two-line/multi-point FLDI signals for the orthogonal configuration.

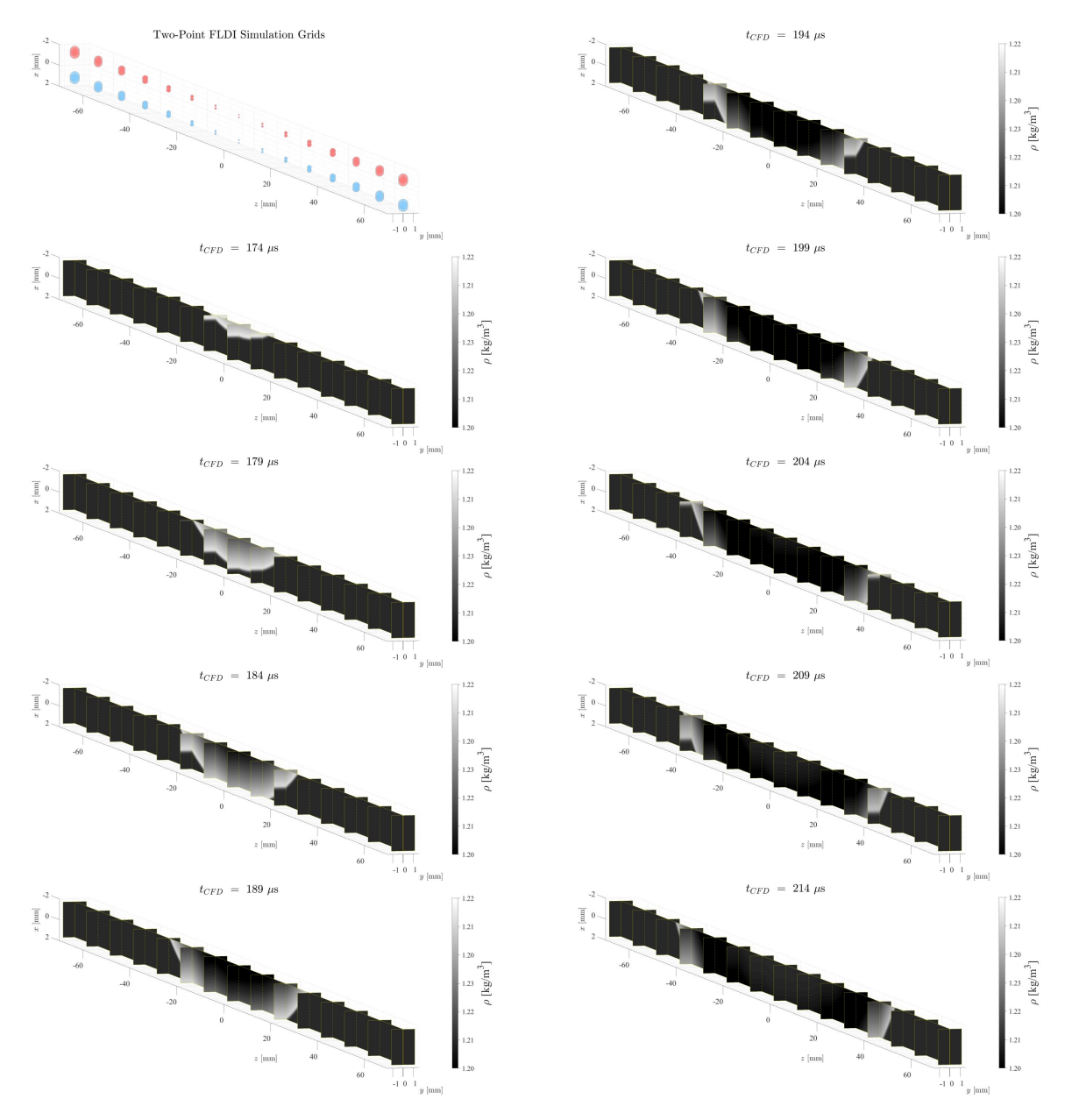


Fig. 7 Notional FLDI simulation grid shown in top-left image with CFD shockwave simulation results beginning 174 μ s after intial laser spark shown in 5 μ s time increments.

In this figure, the time of arrival of the shockwave front is more easily observed, with signals closer to the center of the photodiode array (CH8) peaking earlier than those away from the center (CH2 and CH16). Again, the red and blue curve colors correspond to the Wollaston pair locations relative to the initial LIB spark shown in Fig. 4b. Again, the experimental results will be compared against the simulated FLDI response in the final paper to provide a better understanding of the response of this instrument when operated in the orthogonal configuration.

Acknowledgments

The authors would like to acknowledge Mr. Bill Culliton of the Advanced Measurements and Data Systems Branch at NASA Langley Research Center for his assistance in the design and fabrication of the electrical components for the two-line/multi-point FLDI instrument. The authors would also like to acknowledge the support of the NASA

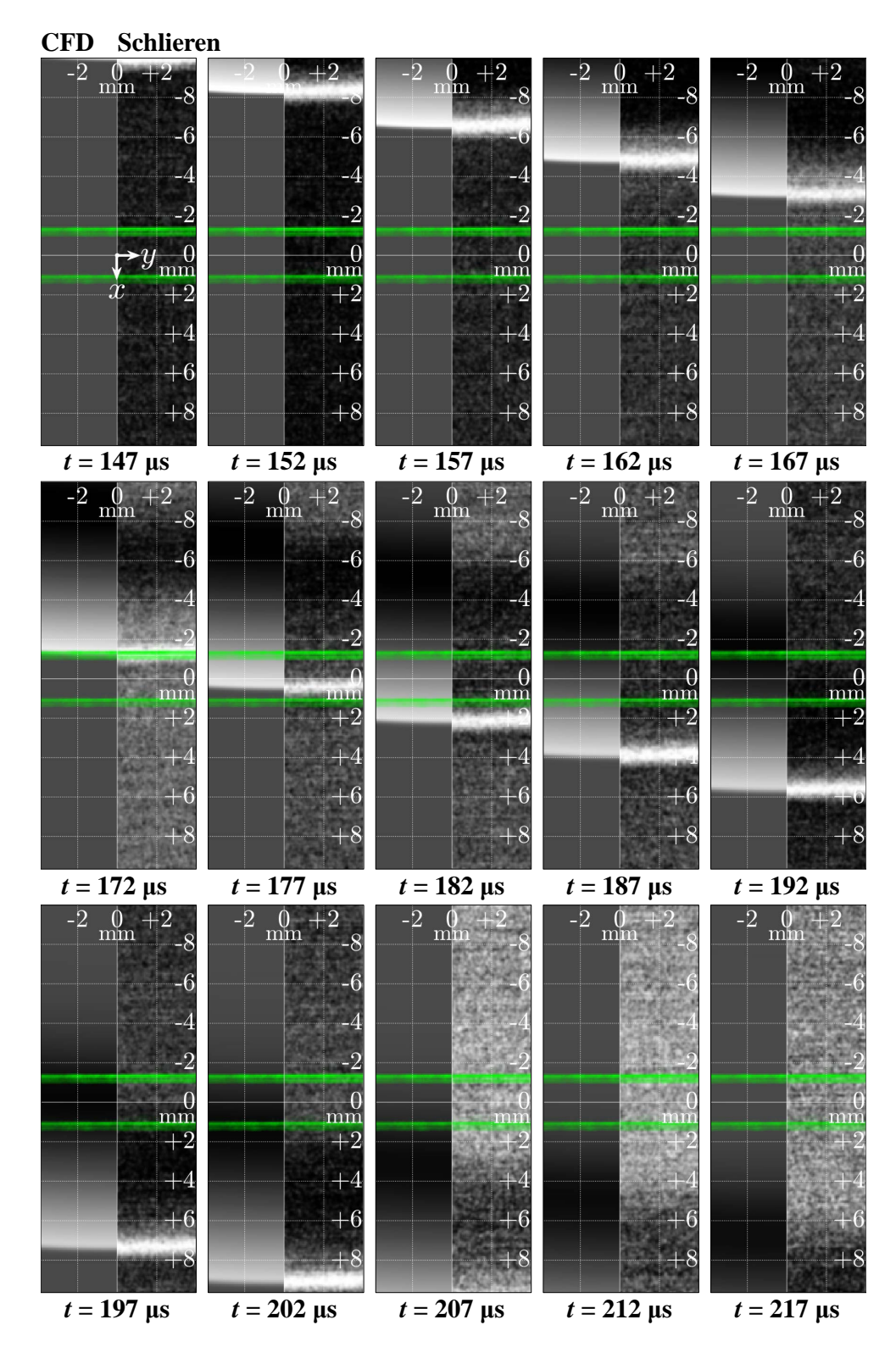


Fig. 8 Comparison of computed density field at z=0 (left) with high-speed schlieren images obtained with a horizontal knife edge (right) at several time steps beginning at $t\approx 147~\mu s$ after the initial laser spark. Focused laser light from two-point FLDI instrument shown in green false color.

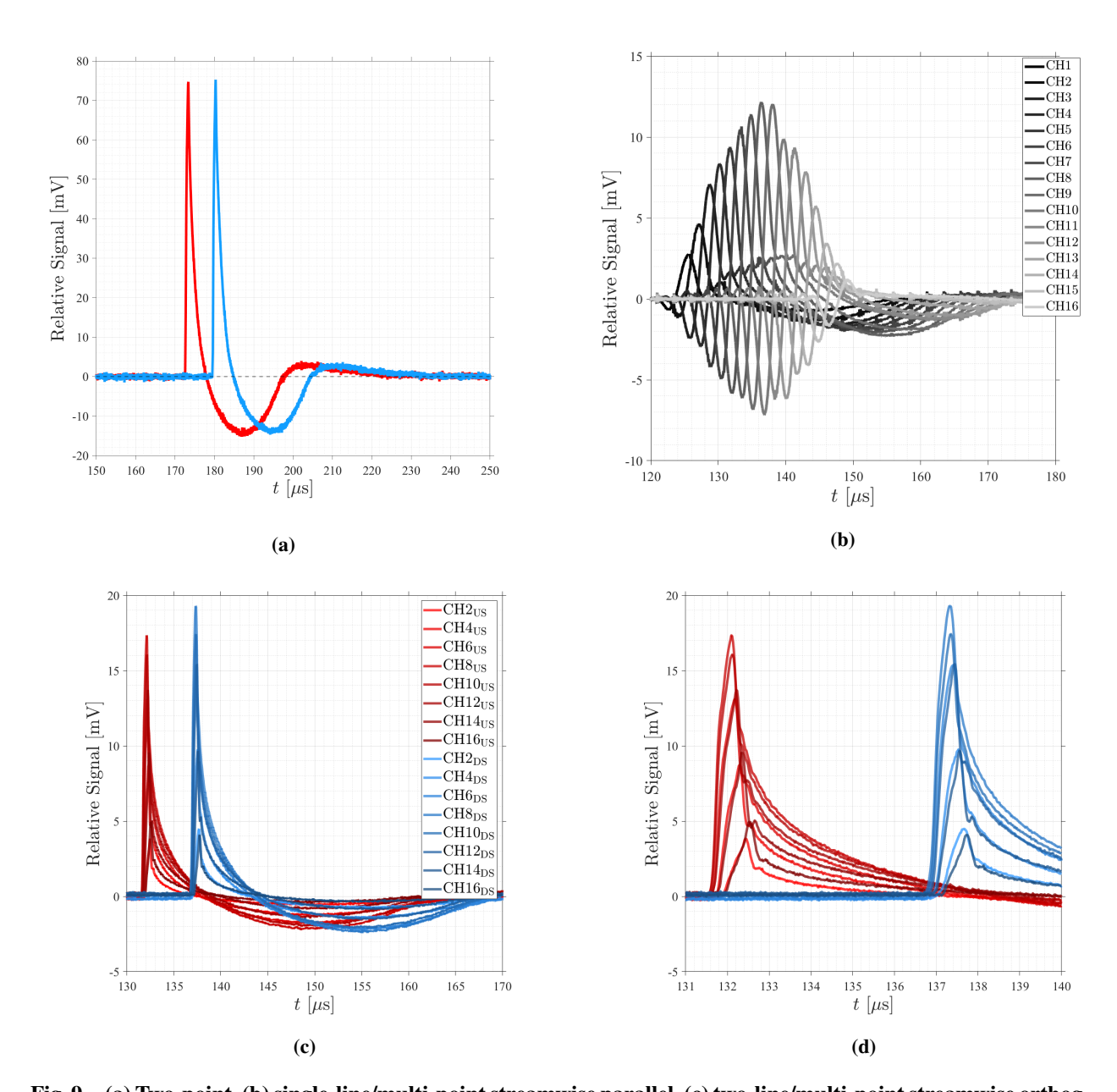


Fig. 9 (a) Two-point, (b) single-line/multi-point streamwise parallel, (c) two-line/multi-point streamwise orthogonal (upstream and downstream Wollaston pairs), and (d) zoomed-in view of two-line/multi-point streamwise orthogonal (upstream and downstream Wollaston pairs) FLDI signals.

Transformational Tools and Technologies (TTT) project and Hypersonic Technologies Project (HTP) for this work.

References

- [1] Smeets, G., and George, A., "Laser-Differential Interferometer Applications in Gas Dynamics," Tech. Rep. 28/73, Institut Franco-Allemand de Recherches Saint-Louis, 1973, Nov. 1973.
- [2] Parziale, N., Shepherd, J., and Hornung, H., "Reflected Shock Tunnel Noise Measurement by Focused Differential Interferometry," 42nd AIAA Fluid Dynamics Conference and Exhibit, American Institute of Aeronautics and Astronautics, 2012.
- [3] Parziale, N. J., Shepherd, J. E., and Hornung, H. G., "Differential Interferometric Measurement of Instability at Two Points in a

- Hypervelocity Boundary Layer," 51st AIAA Aerospac Sciences Meeting Including the New Horizons Forum and Aerospace Exposition, American Institute of Aeronautics and Astronautics, 2013.
- [4] Parziale, N. J., Shepherd, J. E., and Hornung, H. G., "Differential Interferometric Measurement of Instability in a Hypervelocity Boundary Layer," *AIAA Journal*, Vol. 51, No. 3, 2013, pp. 750–754.
- [5] Parziale, N., "Slender-Body Hypervelocity Boundary-Layer Instability," Ph.D. thesis, California Institute of Technology, 05 2013.
- [6] Fulghum, M. R., "Turbulence Measurements in High-Speed Wind Tunnels Using Focusing Laser Differential Interferometry," Ph.D. thesis, The Pennsylvania State University, 12 2014.
- [7] Parziale, N. J., Shepherd, J. E., and Hornung, H. G., "Free-stream density perturbations in a reflected-shock tunnel," *Experiments in Fluids*, Vol. 55, No. 2, 2014, p. 1665.
- [8] Parziale, N. J., Jewell, J. S., Leyva, I. A., and Shepherd, J. E., "Effects of Shock-Tube Cleanliness on Slender-Body Hypersonic Instability and Transition Studies at High Enthalpy," 53rd AIAA Aerospace Sciences Meeting, American Institute of Aeronautics and Astronautics, 2015.
- [9] Parziale, N. J., Shepherd, J. E., and Hornung, H. G., "Observations of hypervelocity boundary-layer instability," *Journal of Fluid Mechanics*, Vol. 781, 2015, pp. 87–112.
- [10] Jewell, J. S., Parziale, N. J., Lam, K.-Y., Hagen, B. J., and Kimmel, R. L., "Disturbance and Phase Speed Measurements for Shock Tubes and Hypersonic Boundary-Layer Instability," 32nd AIAA Aerodynamic Measurement Technology and Ground Testing Conference, American Institute of Aeronautics and Astronautics, 2016.
- [11] Houpt, A., and Leonov, S., "Focused Laser Differential Interferometer for Supersonic Boundary Layer Measurements on Flat Plate Geometries," *AIAA Aviation Forum*, American Institute of Aeronautics and Astronautics, 2018.
- [12] Chou, A., Leidy, A. N., Bathel, B. F., King, R. A., and Herring, G. C., "Measurements of Freestream Fluctuations in the NASA Langley 20-Inch Mach 6 Tunnel," *AIAA Aviation Forum*, American Institute of Aeronautics and Astronautics, 2018.
- [13] Ceruzzi, A., and Cadou, C. P., "Simultaneous Velocity and Density Gradient Measurements using Two-Point Focused Laser Differential Interferometry," AIAA Scitech 2019 Forum, No. 0 in AIAA SciTech Forum, American Institute of Aeronautics and Astronautics, 2019.
- [14] Houpt, A. W., and Leonov, S. B., "Focused and Cylindrical-Focused Laser Differential Interferometer Characterization of SBR-50 at Mach 2," *AIAA Aviation 2019 Forum*, American Institute of Aeronautics and Astronautics, 2019. https://doi.org/10.2514/6.2019-3383.
- [15] Weisberger, J., Bathel, B. F., Jones, S. B., and Herring, G. C., "Focused Laser Differential Interferometry Measurements at NASA Langley 20-Inch Mach 6," AIAA Aviation 2019 Forum, American Institute of Aeronautics and Astronautics, 2019. https://doi.org/10.2514/6.2019-2903.
- [16] Bathel, B. F., Weisberger, J. M., Herring, G. C., King, R. A., Jones, S. B., Kennedy, R. E., and Laurence, S. J., "Two-point, parallel-beam focused laser differential interferometry with a Nomarski prism," *Applied Optics*, Vol. 59, No. 2, 2020, p. 244. https://doi.org/10.1364/ao.59.000244.
- [17] Schmidt, B. E., and Shepherd, J. E., "Analysis of focused laser differential interferometry," *Applied Optics*, Vol. 54, No. 28, 2015, pp. 8459–8472.
- [18] Schmidt, B. E., and Shepherd, J. E., "Analysis of focused laser differential interferometry," *Applied Optics*, Vol. 54, No. 28, 2015, pp. 8459–8472.
- [19] Yan, H., Adelgren, R., Boguszko, M., Elliott, G., and Knight, D., "Laser Energy Deposition in Quiescent Air," *AIAA Journal*, Vol. 41, No. 10, 2003, pp. 1988–1995. https://doi.org/10.2514/2.1888.
- [20] OpenFOAM v7 User Guide, The OpenFOAM Foundation, https://cfd.direct/openfoam/user-guide, 2020.